Millimeter wave imaging system for land mine detection

Todd W. Du Bosq, Jose Manuel Lopez-Alonso, and Glenn D. Boreman

Applications using millimeter wave (mmW) and THz radiation have increased during the past few years. One of the principal applications of these technologies is the detection and identification of objects buried beneath the soil, in particular land mines and unexploded ordnances. A novel active mmW scanning imaging system was developed for this purpose. It is a hyperspectral system that collects images at different mmW frequencies from 90 to 140 GHz using a vector network analyzer collecting backscattering mmW radiation from the buried sample. A multivariate statistical method, principal components analysis, is applied to extract useful information from these images. This method is applied to images of different objects and experimental conditions.

OCIS codes: 100.2980, 110.2960, 120.1880, 120.5700.

1. Introduction

Land mines inflict high costs on civilian populations decades after the military conflicts that prompted their deployment have ceased. The United Nations estimates that over 110 million active mines lie hidden beneath the ground of 68 countries, killing or maiming 2000 people per month. Accidents occur at a rate of one for every 1000 to 2000 mines destroyed.[1] The threat to civilians remains and hinders economic and social recovery.

Antipersonnel mines can be buried just beneath the surface, whereas antitank mines are buried as deep as 40 cm. The land mines can be any shape and can be made of many different materials including metal, plastic, rubber, or wood. There are a number of detection technologies applied for the remediation of minefields, such as inductance coils (metal detectors), magnetometers, ground-penetrating radar, infrared imaging, and explosives vapor sensors.[2] Metallic mines can be detected by using many of the methods mentioned above. However, the increased use of plastic mines has made detection difficult. Inductance coils and magnetometers cannot detect mines with little or no metal content.[3] Ground-penetrating radar systems operate at long wavelengths,[3] which give them high penetration through the soil but low spatial resolution, increasing the false-alarm rate compared with the millimeter wave (mmW) wavelengths. Thermal infrared imaging detection methods require multiple images to be taken 30 min apart to detect the land mines.[4] Explosives vapor sensors often provide poor localization capabilities and spatial resolution.[3] A passive mmW land mine detection system has been demonstrated before,[5] but it depended on the effective sky temperature. An active mmW system[6] is potentially attractive in that, in an imaging mode, it can achieve good discrimination between antipersonnel mines that are primarily nonmetallic, and the small metallic debris (shrapnel and cartridge cases, for example) typical of minefield conditions.

Because of the shape and size discrimination inherent in an imaging system, the trade-off between a false-alarm rate and a miss rate is favorable for mmW wavelengths.[5] The ability to detect and image buried objects will depend on soil transmission and scattering. Soils with particle sizes larger than the wavelength have low transmittance due to scattering.[7] Dry quartz sand has high transmission in the mmW range due to its fairly uniform particle size, which is smaller than the wavelength of light.[7]

A hyperspectral 90–140 GHz mmW imaging system used to locate and identify land mines and other objects buried beneath sand of various depths and conditions is demonstrated. The information provided by the hyperspectral images is analyzed through a principal component analysis (PCA) method. With this signal processing, valuable information is condensed into single images, and the buried objects can be located and identified. The PCA method has been

All the authors are with the University of Central Florida, 4000 Central Florida Boulevard, Orlando, Florida 32816-2700. T. W. Du Bosq (Dubosq@physics.ucf.edu), J. M. Lopez-Alonso, and G. D. Boreman are with the College of Optics and Photonics, CREOL. T. W. Du Bosq and G. D. Boreman are also with the Department of Physics.

Received 21 November 2005; revised 13 February 2006; accepted 20 February 2006; posted 21 February 2006 (Doc. ID 66126).

0003-6935/06/225686-07$15.00/0

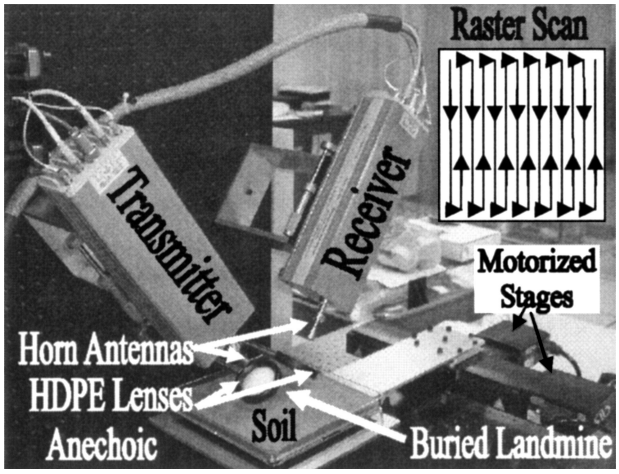

Fig. 1. Photograph of the active hyperspectral mmW imaging system. Inset, schematic of the path for taking a raster scan image. The radiation coming from the transmitter, at 90–140 GHz, is focused onto the sample using the HDPE lens, and scattering radiation from the object is collected and focused on the receiver at each pixel of the raster scan.

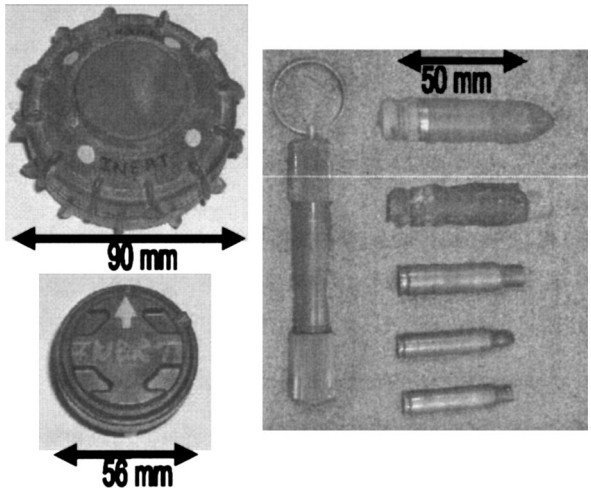

Fig. 2. Photographs of the TS-50 land mine (top left), the M14 land mine (bottom left), and minefield debris (right) including, from top down, a 20 mm OICW practice round, a 20 mm WW II round, a 7.62 mm cartridge case, a 5.56 mm rose crimp cartridge case, and a 5.56 mm standard cartridge case; on the left a fuse lighter with a metal key ring.

used before as a land mine detection signal processing technique in other wavelength regions improving the detection and classification rates while lowering the false-alarm rate.[8–10] We present the experimental setup for the 90–140 GHz mmW imaging system, the signal processing method used, and the imaging results of the buried objects.

2. Experimental Methods

An imaging system was developed for the mmW range by using an Anritsu vector network analyzer (VNA) operating from 90 to 140 GHz. The VNA modules, equipped with 16° horn antennas, were mounted on a vertically oriented optical table, shown in Fig. 1. The mmW radiation was focused by using a high-density polyethylene (HDPE) lens onto the sample and then reflected back through another HDPE lens into the VNA receiver. Two motorized translation stages with 200 mm maximum travel distance and 50 mm/s maximum velocity were mounted perpendicular to each other. The sample was attached to the stages by using a long aluminum arm with the inset removed preventing the sample from being held over the highly reflective metal stages. The land mine was placed in a 20.3 cm $\times$ 20.3 cm $\times$ 9.5 cm container surrounded by soil. This container allowed the land mine to be buried up to 5 cm deep and to be placed anywhere within the 412 cm^2. A broadband convoluted foam mmW absorber, ECCOSORB CV, was placed under the sample to eliminate backreflections from the optical table. A program was written in LabVIEW to capture a raster scan image containing 29 lines (Fig. 1 inset) of the land mine under the soil. At each position of the scan the VNA measured the reflection from the land mine, from 90 to 140 GHz in 1 GHz steps. The resulting data set is converted into a set of images (one for each mmW frequency used) by a MATLAB software program. In our case, the total number of frequencies is 51. The size of the images depends on the number of points taken in each scan and the distance between them. These sizes can be changed with the LabVIEW program.

The objects imaged beneath the soil were two land mines and other minefield debris. The two land mines were the TS-50 (Fig. 2, top left) and the M14 (Fig. 2, bottom left). They are typically scatter laid by a helicopter or buried to a depth of 30 mm.[11] The TS-50 is a circular plastic-body mine with strengthening ribs. The TS-50 has a height of 45 mm, a diameter of 90 mm, and weighs 186 g. It contains a round metallic pressure plate on top of the mine. The TS-50 contains 50 g of T4 explosive and is waterproof and nonbuoyant.[11] The TS-50 cannot be located by using metal detectors under most field conditions and is highly resistant to blast overpressure clearance methods. The M14 land mine is a cylindrical-body plastic mine with very low metal content. The M14 has a height of 40 mm, a diameter of 56 mm, and weighs 90 g. The M14 contains 29 g of tetryl explosive.[11] The M14 is difficult to locate by using metal detectors under most field conditions and can be defeated by using blast overpressure methods. The minefield debris consisted of a 20 mm objective individual combat weapon (OICW) practice round, a 20 mm round from World War II, a 7.62 mm cartridge case, a 5.56 mm rose crimp cartridge case, a 5.56 mm standard cartridge case, and a fuse lighter with a metal key ring (Fig. 2, right panel). The soil sample was quartz sand locally sourced at the University of Central Florida in Orlando, Florida. The soil was dry and maintained in a laboratory environment at about 40% humidity.

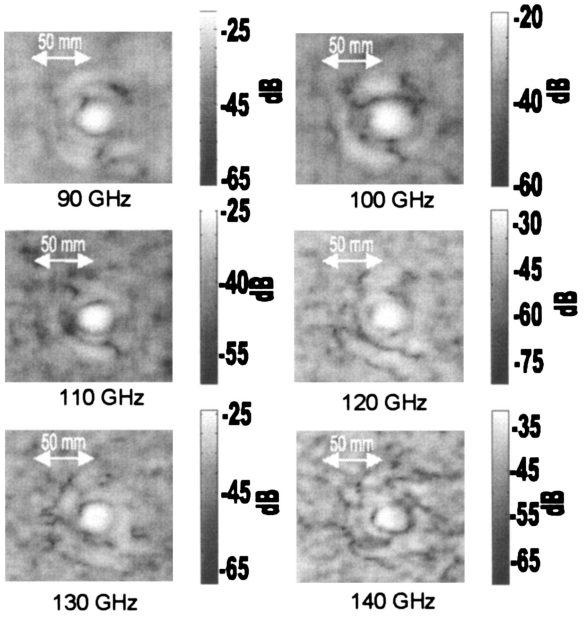

Fig. 3. Six of the 51 single-frequency reflectance images taken from 90 to 140 GHz in 1 GHz steps of the TS-50 land mine with a 2 mm step size, buried 15 mm deep, and with a flat soil surface.

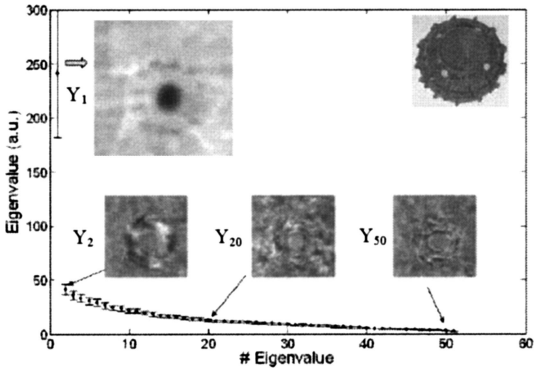

Fig. 4. Application of the PCA to a set of 51 single frequency images of the TS-50 land mine. Only one relevant principal component (Y_1) appears. Some of the higher components (Y_2, Y_{20}, and Y_{50}) are represented.

3. Signal Processing

The initial data set is a collection of N images, each one corresponding to a mmW frequency. Figure 3 shows 6 of the 51 individual images, representing a different frequency, taken during a single scan. The information contained in each image about the object (TS-50 land mine, Fig. 2, top left) is slightly different, and you cannot distinguish whether the object is a land mine, a rock, an aluminum can, or some other minefield debris. The information about the structure of the object is not concentrated around a single frequency but spread over the frequency spectrum. Therefore it is necessary to employ a method that can combine the majority of the available information into a single image with a high signal-to-noise ratio (SNR).

For this purpose, we have used a PCA method. The PCA method is a multivariate statistical method developed primarily to deal with a large ensemble of observations of N random variables.[12] In previous applications, the PCA method was adapted to the case of N images with M points or pixels.[13] In the case of the present work, the original data set is the collection of N images, parameterized by the frequency f, $\{F(x, f)\}_{f=1,\ldots,N}$ where F is a matrix containing all the images and x denotes the spatial coordinate along the scan path within the total of M points. The previous N images are each transformed to produce a mean of zero. Within this framework, the N images are N random variables, and the values of the pixels are random observations. It is easy to calculate the covariance matrix between the N images.[13] In general, this matrix is strongly nondiagonal, which means there is a strong correlation between the images (see Fig. 3). The principal components are a new set of variables (frames) that have no correlation between them. Moreover, the original frames can be seen as a linear combination of the principal components. The coefficients of these linear combinations are obtained through the diagonalization of the frame covariance matrix. This process gives you three outputs: the eigenvalues $\{\sigma_\alpha^2\}_{\alpha=1,\ldots,N}$, the eigenvectors $\{e_\alpha(f)\}_{\alpha=1,\ldots,N}$, and the principal components $\{Y_\alpha\}_{\alpha=1,\ldots,N}$, where α is an integer running from 1 to N. The principal components can be seen as the projections of the original zero mean images into a base produced by the eigenvectors. After diagonalization, there is zero correlation between the principal components Y_α and they are calculated as linear combinations of the original images:

$$Y_\alpha(x) = \sum_{f=1}^{N} e_\alpha(f) F(x, f). \tag{1}$$

But the original images can also be expressed as linear combinations of the principal components:

$$F(x, f) = \sum_{\alpha=1}^{N} e_\alpha(f) Y_\alpha(x). \tag{2}$$

Normally, the principal features of the data set are well represented by a small number of principal components.[14] In our case, the principal features of the land mine are well represented by only one principal component (Y_1 in Fig. 4). This allows the main principal components to be selected and then to reconstruct the original images by using only them, filtering out the higher components. This process is called rectification.[13] One important property of the principal components is that the factor $\sigma_\alpha^2/\sum_{\alpha=1}^{N}\sigma_\alpha^2$ represents the portion of the total variance explained by each principal component. A statistical analysis of the principal component decomposition enables us to classify and group the eigenvalues and the corresponding eigenimages into processes. When a subset of eigenvalues, along with their uncertainty, can be consecutively indistinguishable, they belong to the same process. The uncertainty is produced by the finite size of the data set and the high-order cumulants of

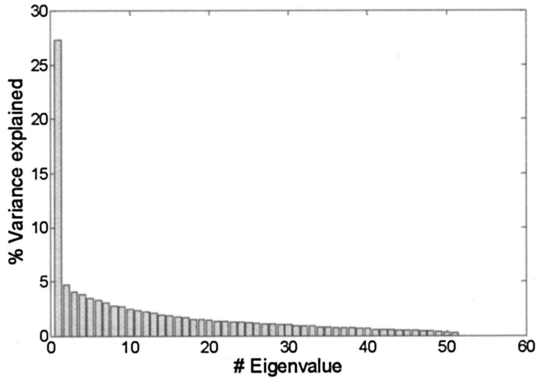

Fig. 5. Percentage of variance explained by the principal components of Fig. 4.

the underlying probability distribution.[13] The advantage of this approach is that it can be implemented automatically. A process is defined as a filtered set of frames generated by a subset of principal components. These processes could contain a single principal component or a large number of them. Based on previous applications of the method to different types of system,[15–17] different types of noise are associated with processes containing a high number of principal components: they are so random that they need a large number of degrees of freedom to describe them. On the other hand, signals normally appear associated to processes with only one principal component or a small number of them.

We have applied the previously described method to the collection of images produced by the mmW imager. After identifying the appearing processes, an analysis of the rectified images for each process is performed. The outputs are related to the physical characteristics of the sample objects. These results are described in Section 4.

4. Results

Figure 4 shows the results of the PCA method for the set of 51 images, some of which are presented in Fig. 3. A relevant principal component clearly appears, and its picture resembles, with high accuracy, the shape of the object buried beneath the sand. The higher principal components are grouped together in a single process, which gives useful information about the structure and composition of the object. Figure 5 represents the total amount of variance explained by each principal component. The first principal component represents only approximately 27% of the total variance.

Two different subdata sets were constructed: the first one coming from the rectification by using only the first principal component, and the second from the rectification by using the higher components. For each subdata set, the mean value and the standard deviation of each pixel is calculated, and three images are constructed: the mean value (signal), the standard deviation (STD), and the ratio of them (the SNR). The results are shown in Fig. 6. The first principal component reconstructs the original shape of

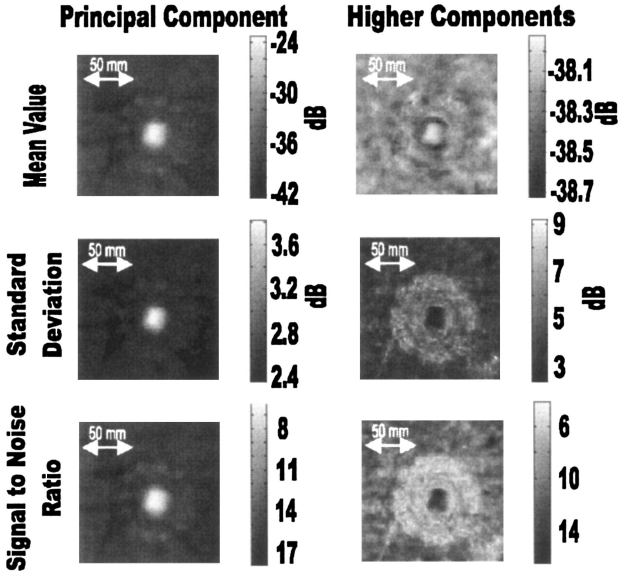

Fig. 6. Images of the mean value, STD, and SNR for the rectified images of Fig. 2 with the first principal component (left) and the higher components (right) of a TS-50 land mine at 2 mm step size, 15 mm deep, and with a flat soil surface.

the object with high accuracy and high SNR (typically 6 to 18). The threshold value of the SNR for which the target is detectable half of the time was determined experimentally in Ref. 18 to be between 2 and 3. The metal inside the mine is clearly seen in the signal, meaning that the metal reflection drives it. However, reflections from the plastic body of the mine showing the structure of the strengthening ribs are seen. We also reconstruct the data using the remaining components (the higher components) and perform the same analysis as before, obtaining the signal, the STD, and the SNR. In the reconstruction with the higher components, the signal is weaker, but the standard deviation is high. The difference in the structure and material of the background and object is responsible for this behavior. The plastic part of the object is curved, and the reflection changes with the angle, while the background is random. Also, the reflection from the plastic varies at different frequencies, which will be represented by the higher order components. This is the reason the STD of the higher-order components is greater than the STD of the first principal component. The main difference is that, while a strong signal is produced mainly by metal components of the object, the structure in the higher components is driven mainly by the structure of the plastic material.

A. Other Types of Objects

Antipersonnel mines vary widely in size, shape, and material content depending on their intended use and burial location. The PCA method was applied to other land mines and minefield debris. The M14 land mine has a different size and shape compared with the TS-50 as well as a much smaller metal content. Images were taken for the M14 land mine with a 2 mm step size, buried 15 mm deep, and with a flat

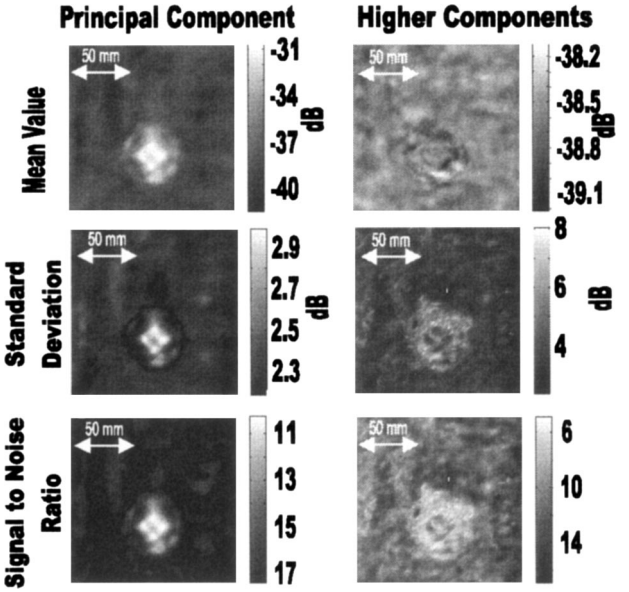

Fig. 7. Images of the mean value, STD, and SNR for the rectified images of an M14 land mine with the first principal component (left) and the higher components (right) at 2 mm step size, 15 mm deep, and with a flat soil surface.

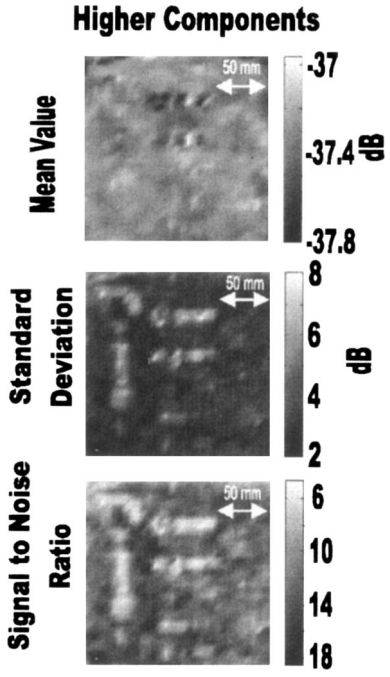

Fig. 8. Images of the mean value, STD, and SNR for the rectified images of the minefield debris with the higher components at 2 mm step size, 15 mm deep, and with a flat soil surface. The principal component rectified images did not show any features of the objects.

soil surface. As with the previous mine, the PCA method allows the structure and composition of the mine to be identified. The results are given in Fig. 7. The unique structure of the top cap of the mine can be identified from the principal component images. The higher component images show the plastic composition of the land mine. The percentage of variance explained by the first principal component is similar to the previous case.

Figure 8 shows the results of the analysis for a collection of bullet cartridges and other types of minefield debris. In this case, the object is not visible in the first principal component but in the STD of the reconstruction with the higher components. The curvature of the objects introduces deviations in the reflection coefficients. In the previous images, the metal was large and planar compared with the wavelength, which produces strong reflections. In this case, the dimensions of the metal parts are small or comparable to the wavelength, producing small backscattering. The objects are curved and have reflection changes that introduce a high STD. The PCA method can even distinguish between objects with such small fluctuations allowing the minefield debris to be located and identified.

B. Resolution, Depth, and Soil Surface

The influences of other physical characteristics related to mine detection were explored. These factors include image resolution, depth of the object, and the condition of the soil surface. For this study the TS-50 land mine analyzed earlier in Section 2 was selected. In all cases, the level of the first principal components is between 25% and 30% of the total data set variance.

Figure 9 shows the images of the TS-50 land mine when the resolution of the scan is 5 mm steps with a depth of 15 mm and the soil surface flat. This figure can be compared to Fig. 6 (2 mm steps, 15 mm depth, and flat soil surface). The added resolution from a step size of 5 to 2 mm does not change the overall image significantly. The 2 mm step size oversamples the image without adding useful information while

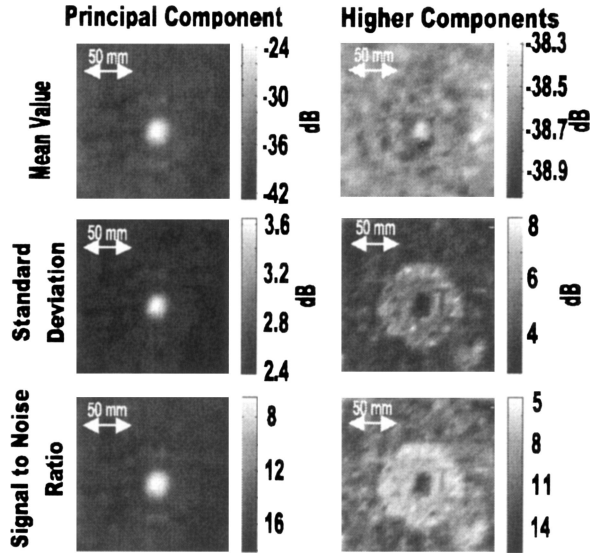

Fig. 9. Change in resolution. Images of the mean value, STD, and SNR for the rectified images of a TS-50 land mine with the first principal component (left) and the higher components (right) at 5 mm step size, 15 mm deep, and with a flat soil surface.

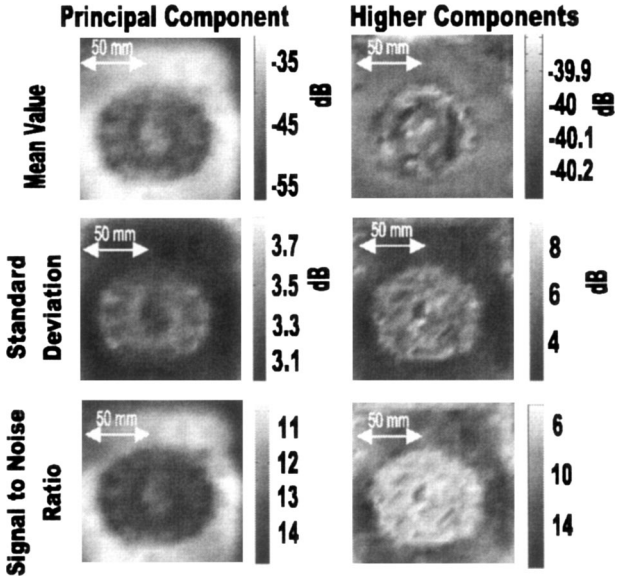

Fig. 10. Change in depth. Images of the mean value, STD, and SNR for the rectified images of a TS-50 land mine with the first principal component (left) and the higher components (right) at 5 mm step size, 50 mm deep, and with a flat soil surface.

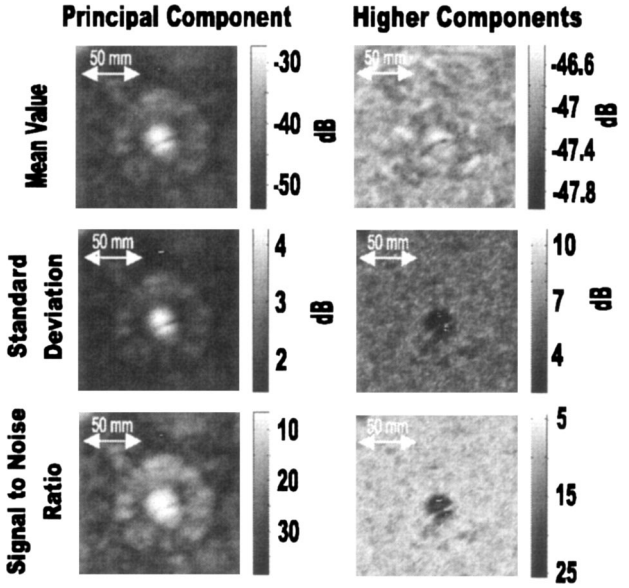

Fig. 11. Change in soil surface. Images of the mean value, STD, and SNR for the rectified images of a TS-50 land mine with the first principal component (left) and the higher components (right) at 2 mm step size, 15 mm deep, and with a disturbed soil surface.

adding time to complete the scan. The spot size of the imaging system is approximately 5 mm; therefore it is sufficient to use a 5 mm step size while taking images, since our system is not a subdiffraction limited–superresolution process.

The images of the TS-50 land mine buried at a depth of 50 mm with 5 mm steps and a flat soil surface is shown in Fig. 10. This figure can be compared with Fig. 9 (5 mm step size, 15 mm depth, and flat soil surface). Changing the depth affects the images in two ways. First, the radiation has to travel a longer distance in the random soil, increasing the effects of scattering, which decreases the reflected signal from the object. Second, the uncertainties related to the beam focus are increased causing a blur over the object. However, the PCA method can extract information from the first principal component and higher components locating and identifying the land mine. Due to the depth of the land mine compared with the size of the container and the orientation of the VNA modules, the edges of the container can be seen in Fig. 10.

Figure 11 shows the images of the TS-50 land mine with a 2 mm step size at a depth of 15 mm with a disturbed soil surface. This figure can be compared with Fig. 6 (2 mm step size, 15 mm depth, and a flat soil surface). The images of the flat soil surface and the disturbed soil surface show a comparison between an ideal smooth surface and a real-world type of situation where the surface above the mine is disturbed. The disturbed surface introduces a blur in the image and increases the effects of scattering while largely destroying the useful information in the higher components. The land mine is detected and identified with the disturbed surface, degrading only the information in the higher components about the plastic in the mine. It is important to note that in both cases the maximum signal level, STD, and SNR are similar. This supports the idea that disturbed surface soil can be modeled as a blur or scattering imposed over the image.

5. Conclusions

An experimental 90–140 GHz mmW imaging system was developed and tested by using different types of object. The principal application was the detection of land mines and minefield debris buried in soil. The final data set was a collection of mmW images at different frequencies. A signal processing method based on a principal component analysis was applied to the images to separate different structures that help to identify the objects. In most cases, the first principal component appeared strongly related to the structure of the object. Information in the higher components was also extracted giving additional information about the composition of the object. The mmW imaging system and the PCA method were successful as a means of locating and identifying the objects buried beneath the soil. Image resolution, depth of the object, and the condition of the soil surface were explored. Changing the image resolution from a 2 to a 5 mm step size did not degrade the image significantly and allowed a quicker scan. As the depth was increased from 15 to 50 mm, the buried object was still located and identified. The object was also located and identified with a disturbed soil surface similar to a real-world situation. A hyperspectral mmW imaging system using the PCA method is a promising technique for the detection of land mines and unexploded ordnances.

We thank Mark Cumo of the U.S. Army Night Vision and Electronic Sensors Directorate for providing the land mines used in this study. This work was supported by Northrop Grumman Corporation, Integrated Systems Division, Melbourne, Florida.

References and Notes

1. "Landmines Fact Sheet," United Nations Mine Clearance and Policy Unit, Department of Humanitarian Affairs, United Nations, September 1997, http://www.un.org/Pubs/CyberSchoolBus/banmines/facts.asp.
2. K. Kowalenko, "Saving lives, one land mine at a time," The Institute **28,** 10–11 (2004).
3. M. Acheroy, "Mine action: status of sensor technology for close-in and remote detection of antipersonnel mines," in *Proceedings of the Third International Workshop on Advanced Ground Penetrating Radar* (Delft, Netherlands, 2005), pp. 3–13.
4. M. Schachne, L. van Kempen, D. Milojevic, H. Sahli, Ph. Van Ham, M. Acheroy, and J. Cornelis, "Mine detection by means of dynamic thermography: simulation and experiments," in *The Second International Conference on the Detection of Abandoned Landmines* (1998), pp. 124–128.
5. L. Yujiri, B. Hauss, and M. Shoucri, "Passive millimeter wave sensors for detection of buried mines," in *Detection Technologies for Mines and Minelike Targets,* A. Dubey, I. Cindrich, J. Ralston, and K. Rigano, eds., Proc. SPIE **2496,** 2–6 (1995).
6. H. Zhong, N. Karpowicz, J. Partridge, X. Xie, J. Xu, and X.-C. Zhang, "Terahertz wave imaging for landmine detection," in *Terahertz for Military and Security Applications II,* R. J. Hwu and D. L. Woolard, eds., Proc. SPIE **5411,** 33–44 (2004).
7. T. W. Du Bosq, R. E. Peale, and G. D. Boreman, "Terahertz/millimeter wave characterizations of soils for mine detection: transmission and scattering," IEEE Trans. Geosci. Remote Sens. (submitted for publication, 2005).
8. X. Miao, M. R. Azimi-Sadjadi, B. Tian, A. C. Dubey, and N. H. Witherspoon, "Detection of mines and minelike targets using principal component and neural-network methods," IEEE Trans. Neural Netw. **9,** 454–463 (1998).
9. M. R. Azimi-Sadjadi, D. E. Poole, S. Sheedvash, K. D. Sherbondy, and S. A. Stricker, "Detection and classification of buried dielectric anomalies using a separated aperture sensor and a neural network discriminator," IEEE Trans. Instrum. Meas. **41,** 137–143 (1992).
10. B. Karlsen, J. Larsen, H. B. D. Sorensen, and K. B. Jakobsen, "Comparison of PCA and ICA based clutter reduction in GPR systems for anti-personal landmine detection," in *Proceedings of IEEE Conference on Statistical Signal Processing* (IEEE 2001), pp. 146–149.
11. "Landmine Data Sheet," National Defence Mine/Countermine Information Centre, The Department of National Defence, August 2005, http://ndmic-cidnm.forces.gc.ca.
12. D. F. Morrison, *Multivariate Statistical Methods,* 3rd ed. (McGraw-Hill 1990).
13. J. M. Lopez-Alonso, J. Alda, and E. Bernabeu, "Principal components characterization of noise for infrared images," Appl. Opt. **41,** 320–331 (2002).
14. J. Kositsky, R. Cosgrove, C. Amazeen, and P. Milanfar, "Results from a forward-looking GPR mine detection system," in *Detection and Remediation Technologies for Mines and Minelike Targets VII,* J. T. Broach, R. S. Harmon, and G. J. Dobeck, eds., Proc. SPIE **4742,** 206–217 (2002).
15. W. R. Folks, J. M. Lopez-Alonso, B. Monacelli, A. Weeks, G. Zummo, D. Mullally, and G. D. Boreman, "Characterization of digital-micromirror device-based infrared scene projector," Opt. Eng. **44,** 086402 (2005).
16. J. M. Lopez-Alonso, B. Monacelli, J. Alda, and G. Boreman, "Uncertainty analysis in the measurement of the spatial responsivity of infrared antennas," Appl. Opt. **44,** 4557–4568 (2005).
17. J. M. Lopez-Alonso, J. M. Rico-Garcia, and J. Alda, "Photonic crystal characterization by FDTD and principal component analysis," Opt. Express **12,** 2176–2186 (2004).
18. D. Schumaker, J. Wood, and C. Thacker, *Infrared Imaging Systems Analysis* (DCS Corporation, 1998).